High-Temperature Deformation Behavior of a Gamma TiAl Alloy—Microstructural Evolution and Mechanisms

JEOUNG HAN KIM, TAE KWON HA, YOUNG WON CHANG, and CHONG SOO LEE

The present investigation was carried out in the context of the internal-variable theory of inelastic deformation and the dynamic-materials model (DMM), to shed light on the high-temperature deformation mechanisms in TiAl. A series of load-relaxation tests and tensile tests were conducted on a fine-grained duplex gamma TiAl alloy at temperatures ranging from 800 °C to 1050 °C. Results of the load-relaxation tests, in which the deformation took place at an infinitesimal level ($\varepsilon \cong 0.05$), showed that the deformation behavior of the alloy was well described by the sum of dislocation-glide and dislocation-climb processes. To investigate the deformation behavior of the fine-grained duplex gamma TiAl alloy at a finite strain level, processing maps were constructed on the basis of a DMM. For this purpose, compression tests were carried out at temperatures ranging from 800 °C to 1250 °C using strain rates ranging from 10 to 10^{-4}/s. Two domains were identified and characterized in the processing maps obtained at finite strain levels (0.2 and 0.6). One domain was found in the region of 980 °C and 10^{-3}/s with a peak efficiency (maximum efficiency of power dissipation) of 48 pct and was identified as a domain of dynamic recrystallization (DRx) from microstructural observations. Another domain with a peak efficiency of 64 pct was located in the region of 1250 °C and 10^{-4}/s and was considered to be a domain of superplasticity.

I. INTRODUCTION

CONSIDERABLE research work has been carried out during the last two decades to develop high-temperature structural materials with excellent creep resistance as well as good oxidation resistance. Gamma (γ)–based TiAl alloys are an attractive material satisfying these requirements[1] and could be used for parts such as airplane turbine blades, transition duct beams, vanes, and nozzle flaps.[2,3] However, the material is brittle at ambient temperatures and is difficult to work at high temperatures. Accordingly, many investigations have been conducted into the source of brittleness and to enhance the ductility and hot workability by the addition of other alloying elements and/or by control of the microstructure.[4,5]

Previous studies on the high-temperature deformation behavior of TiAl alloys have been mainly focused on (1) the identification of the mechanisms responsible for the ductile-brittle transition observed at approximately 600 °C, (2) the assessment of the plastic-flow and fracture properties, and (3) the development of processing maps to establish strain-rate/temperature regimes where sound material can be obtained.[6–9] To date, most of the earlier work has investigated the plastic-flow behavior of TiAl using power-law relationships ($\sigma = K\,\dot{\varepsilon}^m$) or the Zener–Holloman parameter, which is phenomenological in nature. In the earlier work, the predominant deformation mechanisms operating at specific temperatures, which may include dislocation glide, dislocation climb, and grain-boundary sliding, have not been well defined. In addition, a processing map for TiAl alloys that indicates optimized hot-working conditions has not been reported yet, and only the isostress contour map has been made to show the region of sound deformation from an engineering viewpoint.[9] Important information such as the working efficiency or optimum hot-working conditions cannot be understood from this approach.

To gain an understanding of the aforementioned issues, the high-temperature deformation characteristics of a TiAl alloy were analyzed in the context of the internal-variable theory of inelastic deformation proposed by Ha and Chang[10] and the dynamic materials model (DMM) proposed by Prasad and Sasidhara.[11] The former provides a promising framework for describing the deformation behavior at an infinitesimal strain level and has been successfully applied to high-temperature deformation of Ti-6Al-4V and Ti_3Al-xNb alloys.[12,13] The latter, on the other hand, is very effective in describing a deformation behavior at high strain levels, where the dynamic processes such as dynamic recovery and dynamic recrystallization (DRx) can occur.

II. INTERNAL-VARIABLE THEORY OF INELASTIC DEFORMATION

Figure 1 shows a rheological and a topological model for inelastic deformation, including grain-matrix deformation (GMD) and grain-boundary sliding (GBS). The former comprises plastic deformation due to a dislocation-glide process giving rise to an internal strain (a) and nonrecoverable plastic stain (α) and a dislocation-climb process (β). For the model shown in Figure 1, the following stress and kinematic relations among the rate variables can be derived:

$$\sigma = \sigma^I + \sigma^F \qquad [1]$$

JEOUNG HAN KIM, Graduate Ph.D. Candidate Student, and YOUNG WON CHANG and CHONG SOO LEE, Professors, are with the Center for Advanced Aerospace Materials and the Department of Materials Science and Engineering, Pohang University of Science and Technology, Pohang 790-784, Korea. TAE KWON HA, Researcher, is with the Research Institute of Industrial Science and Technology, Pohang 790-600, Korea.

This article is based on a presentation made in the symposium entitled "Fundamentals of Structural Intermetallics," presented at the 2002 TMS Annual Meeting, February 21-27, 2002, in Seattle, Washington, under the auspices of the ASM and TMS Joint Committee on Mechanical Behavior of Materials.

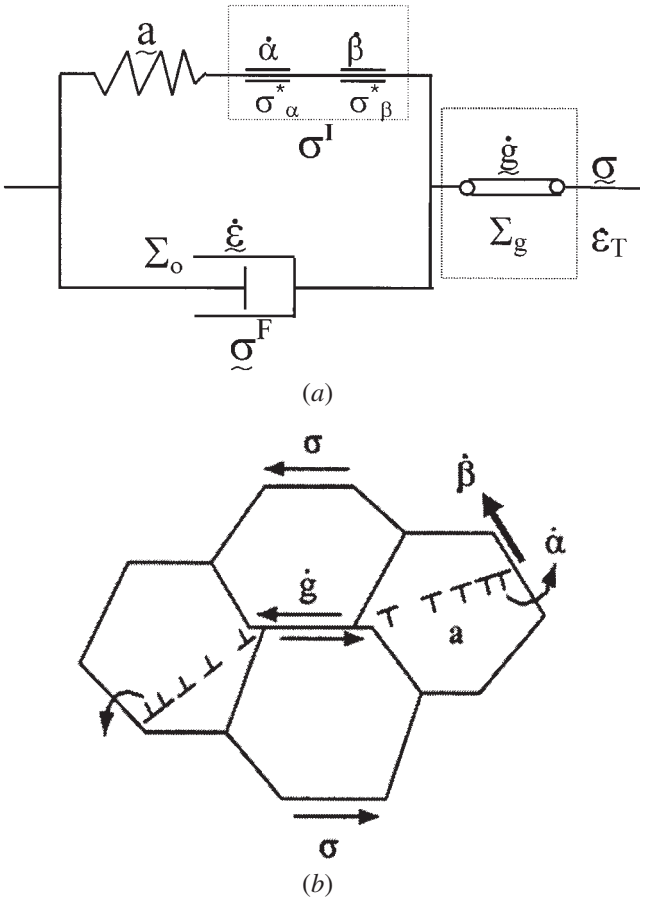

Fig. 1—An internal variable model for describing high-temperature deformation: (*a*) a rheological model and (*b*) a topological model.

$$\dot{\varepsilon}_T = \dot{a} + \dot{\alpha} + \dot{\beta} + \dot{g} \qquad [2]$$

where $\dot{\alpha}$, $\dot{\beta}$, and $\dot{g}$ denote the plastic strain rates due to dislocation glide, dislocation climb, and GBS, respectively. The variables σ^I and σ^F are the internal stress due to the long-range interaction among dislocations and the friction stress due to the short-range interaction between a dislocation and the lattice, respectively. At the high temperatures used in this study, σ^F is, in general, very small as compared to σ^I, and the internal strain rate ($\dot{a}$) can be neglected for load-relaxation tests performed under steady-state conditions. Therefore, it is sufficient to describe the constitutive relation at high temperatures using the $\dot{\alpha}$, $\dot{\beta}$, and $\dot{g}$ elements (Figure 1).

The constitutive relation for the plastic strain rate ($\dot{\alpha}$) can be formulated as a kinetic equation which describes the mechanical activation process of the leading dislocation by the internal stress. For uniaxial tension, the scalar relation is expressed in a form similar to that of Lee and Hart,[14] *i.e.*,

$$(\sigma_\alpha^*/\sigma^I) = \exp\,(\dot{\alpha}^*/\alpha)^p \qquad [3]$$

$$\dot{\alpha}^* = v^I(\sigma_\alpha^*/G)^{n^I} \exp\,(-Q_\alpha{}^I/RT) \qquad [4]$$

where p and n^I are material constants, and $\sigma_\alpha{}^*$ and $\dot{\alpha}^*$ denote the internal-strength variable and its conjugate reference strain rate, respectively. Equation [4] represents an activation relation for dislocations at grain boundaries, with v^I denoting the jump frequency, $Q_\alpha{}^I$ denoting the activation energy, and G denoting an internal modulus.

Grain-boundary sliding can be represented as stress-induced viscous flow under a frictional drag; thus, the following scalar relation between the applied stress and GBS rate can be derived:

$$(\dot{g}/\dot{g}_0) = ((\sigma - \Sigma_g)/\Sigma_g)^{1/M_g} \qquad [5]$$

$$\dot{g}_0 = v^g(\Sigma_g/\mu^g)^{n^g} \exp\,(-Q^g/RT) \qquad [6]$$

where M_g and n^g are material constants and Σ_g and $\dot{g}_0$ are the static friction stress and its conjugate reference rate for GBS, respectively. Equation [6] also represents a thermally activated process of GBS, with Q^g denoting the activation energy for GBS.

Like the plastic strain rate $\dot{\alpha}$, the strain rate due to the dislocation-climb process, $\dot{\beta}$, can be formulated as follows:[15]

$$(\sigma_\beta^*/\sigma^I) = \exp\,(\dot{\beta}^*/\dot{\beta})^p \qquad [7]$$

$$\dot{\beta}^* = v^I(\sigma_\beta^*/G)^{n^I} \exp\,(-Q_\beta^I/RT) \qquad [8]$$

III. EXPERIMENTAL PROCEDURES

The gamma-TiAl alloy used in this study was supplied by UES, Inc. (Dayton, OH) in the form of a 14-mm-thick pancake forging. The chemical composition of the material was Ti-46Al-1.9Cr-3.0Nb-0.18W-0.16B-0.13C, in at. pct. To obtain fine equiaxed microstructures, the as-received material was heat treated at 1280 °C for 3 hours, followed by furnace cooling to 800 °C, air cooling to room temperature, and, finally, aging at 900 °C for 24 hours. Figure 2(a) shows an optical micrograph of the resulting microstructure, which is a duplex structure with an average gamma grain size of ~13 μm. Annealing twins were observed in the microstructure after the heat treatment. Figure 2(b) shows a backscattered electron (BSE) image of the resulting microstructure. Three phases were observed in the BSE image: γ (dark), α_2 (light gray), and β (white). The α_2 grains were distributed between γ grain boundaries, and its volume fraction was measured to be about 8 to 10 pct. The β grains were dispersed as small particles or films with a small volume fraction of ~2 pct.

Load-relaxation tests were performed to obtain flow curves and pertinent constitutive parameters at temperatures between 800 °C and 1020 °C. Tensile tests were carried out using an Instron 1361 testing machine with a three-zone furnace capable of maintaining the temperature constant within ±0.5 °C. All tests were conducted in argon gas to minimize oxidation. The gage dimensions of the test specimens were 27 mm in length, 4 mm in width, and 3 mm in thickness. The load-time ($P-t$) curves were converted to flow stress *vs* strain rate ($\sigma-\dot{\varepsilon}$) by applying the methods proposed by Lee and Hart.[14] As evidenced by microstructural analysis, the microstructure did not significantly change after the load-relaxation tests.

The high-temperature compression tests were conducted in a vacuum of 10^{-1} torr at temperatures between 800 °C and 1250 °C at constant strain rates within the of range 10^{-4}/s and 10/s. Cylindrical specimens, with a diameter of 8 mm and a height of 12 mm, were machined by electrodischarge machining. Specimens were heated by induction coils at a heating rate of 5 °C/s and were soaked for 300 seconds at the test temperature before the tests were performed. The

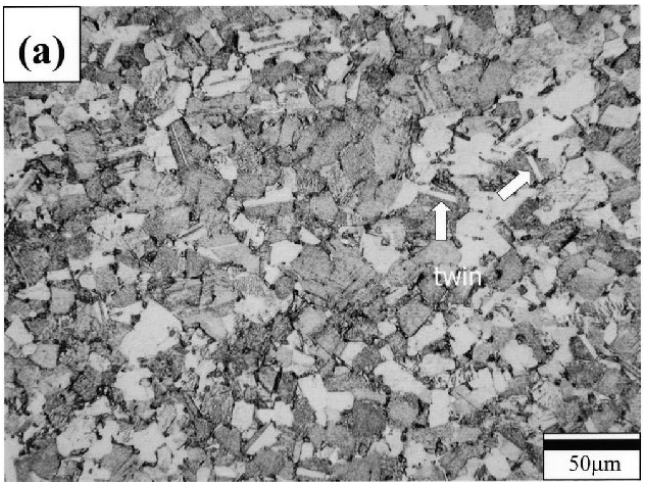

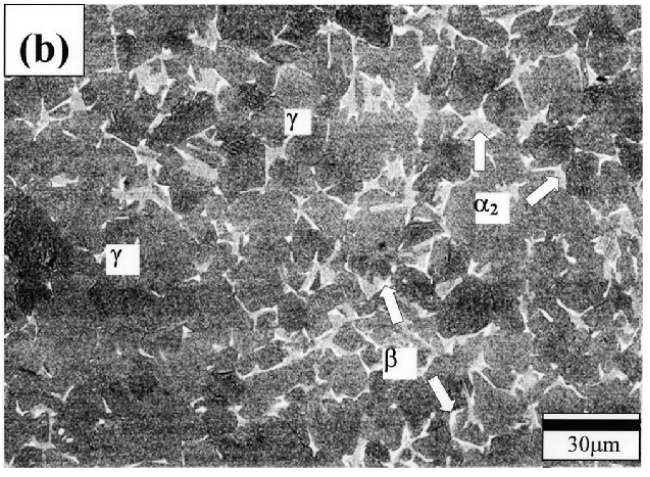

Fig. 2—Initial microstructure of heat-treated TiAl specimen: (*a*) optical image and (*b*) backscattered electron image.

true stress–true strain curves were obtained from the load-displacement data. In order to investigate the microstructural evolution during the deformation, the specimens were quenched from the test temperatures immediately after the deformation using liquid nitrogen. The microstructures of the deformed specimens were analyzed to verify the results of the DMM analysis.

IV. RESULTS

A. *Stress-Strain–Rate Curves Obtained by Load-Relaxation Test ($\varepsilon \cong 0.05$)*

Stress *vs* strain rate curves for the duplex TiAl alloy obtained from the load-relaxation tests at various temperatures are shown in Figure 3. It is apparent that the curves shifted progressively toward the region of lower stress and higher strain rate as the temperature increased. It is also noted that the flow stress obtained at high temperatures (above 980 °C) decreased rapidly in the low-strain-rate region (below 10^{-5}/s).

The data for the low-temperature tests (800 °C and 880 °C) fitted well with Eq. [3], which describes dislocation glide. The solid lines in Figure 4 are the fitting lines based on Eq. [3], with the constitutive parameters obtained using a nonlinear regression method. The constitutive parameters (σ_α*, $\dot{\alpha}$*, and p) for dislocation glide are summarized in Table I. At 980 °C and 1020 °C, the experimental data (Figures 4(c) and (d)) deviated from the dislocation-glide lines of Eq. [3], especially in the lower-strain-rate region, thus implying that another deformation mode was operating along with dislocation glide. Among several possibilities, the dislocation-climb process (β element) was considered to be the most probable in this temperature range.[16,17] The grain-boundary-sliding rate ($\dot{g}$) was assumed to be zero, because the stress-strain–rate curves did not reveal any concave downward shape, which would result from the operation of GBS.[10,18,19] To separate out the portion of dislocation climb, the values of strain rate for the dislocation-climb process were estimated from Eq. [7]. These values were subsequently used during a nonlinear curve fitting of Eq. [7] to determine the constitutive parameters (σ_β*, $\dot{\beta}$*, and p) for the dislocation-climb process. The dotted lines in Figures 4(c) and (d) represent the predicted curves for the dislocation-climb process. The combined curves of GMD ($\dot{\alpha} + \dot{\beta}$) were compared with the experimental data, and excellent agreement was found. The constitutive parameters above 900 °C are also summarized in Table I. The parameter p, characterizing the dislocation permeability of strong barriers, was determined to be 0.15, a value similar to those found in other fcc and bcc materials.[15,18]

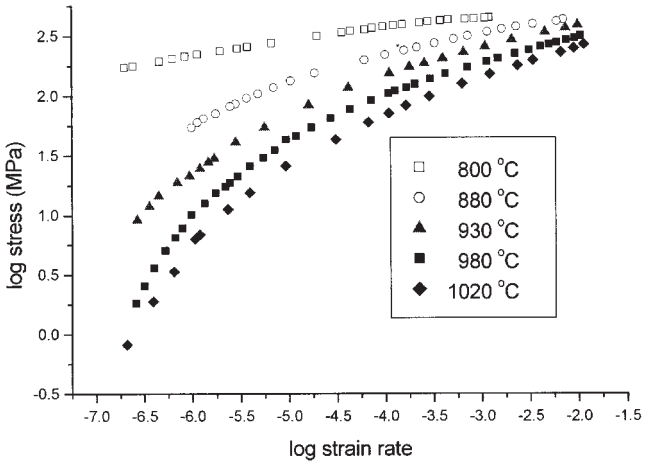

Fig. 3—The flow stress-strain rate curves of TiAl alloy obtained by load-relaxation tests at various temperatures.

B. *Stress-Strain Curves Obtained by Hot Compression Tests*

The true stress-true strain curves obtained at a constant strain rate of 10^{-3}/s for different temperatures and those obtained at a constant temperature of 980 °C with different strain rates are shown in Figure 5. In Figure 5(a), the stress-strain curves at 800 °C exhibited nearly steady-state behavior, while flow softening occurred at higher temperatures (900 °C to 1050 °C). However, as the temperature increases above 1150 °C, the flow softening

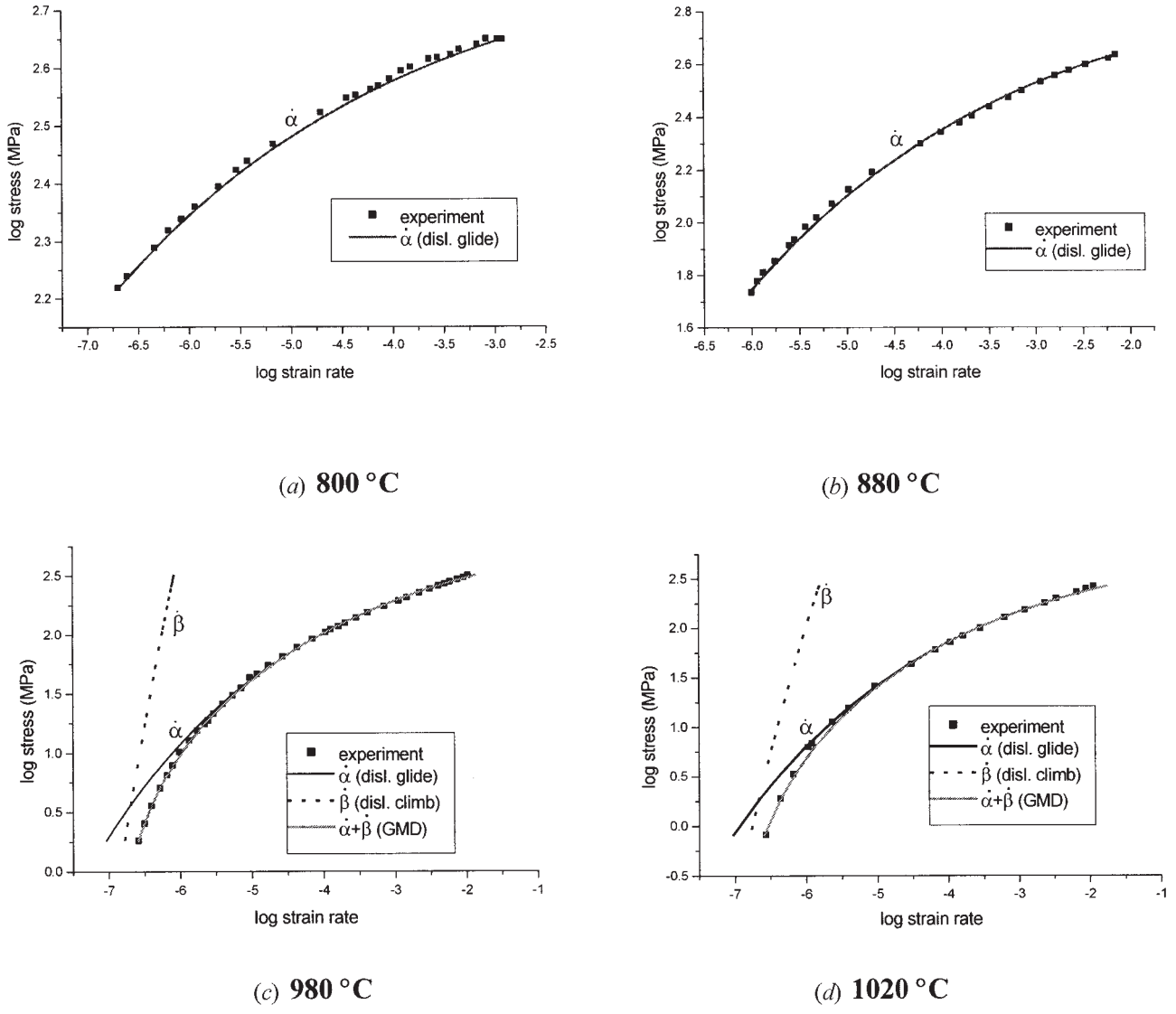

Fig. 4—(*a*) through (*d*) Experimental flow data (■) obtained by load relaxation tests and predicted curves based on the internal variable theory.

Table I. Constitutive Parameters Determined from Load-Relaxation Tests at Various Temperatures

	Dislocation Glide			Dislocation Climb		
Temperature (°C)	Log σ_α*	Log $\dot{\alpha}$*	p	Log σ_β*	Log $\dot{\beta}$*	p
880	2.958	−3.030	0.15	—	—	0.15
930	2.971	−2.233		6.864	0.274	
950	2.950	−2.159		6.937	0.920	
980	2.934	−1.822		7.560	1.251	
1020	2.911	−1.428		7.788	1.451	

disappeared and steady-state behavior reappeared. From these results, it is expected that some softening mechanism operated over the temperature regime between 900 °C and 1050 °C.

In Figure 5(b), flow curves obtained from high-strain-rate conditions (above 10^{-1}/s) exhibited work hardening at the early stage of deformation and then gradual softening occurred at a strain above 0.2, which was found to be due to a dynamic recovery process. In particular, the flow stress of the curve at 980 °C and 10/s decreased rapidly after work hardening, which was attributed to surface cracking during deformation. This will be discussed in a later section. On the other hand, flow curves obtained under low-strain-rate conditions (below 10^{-2}/s) did not exhibit any work-hardening behavior; the flow stress decreased continuously and reached a steady state with increasing strain. The flow-stress data as a function of temperature, strain rate, and strain are given in Table II.

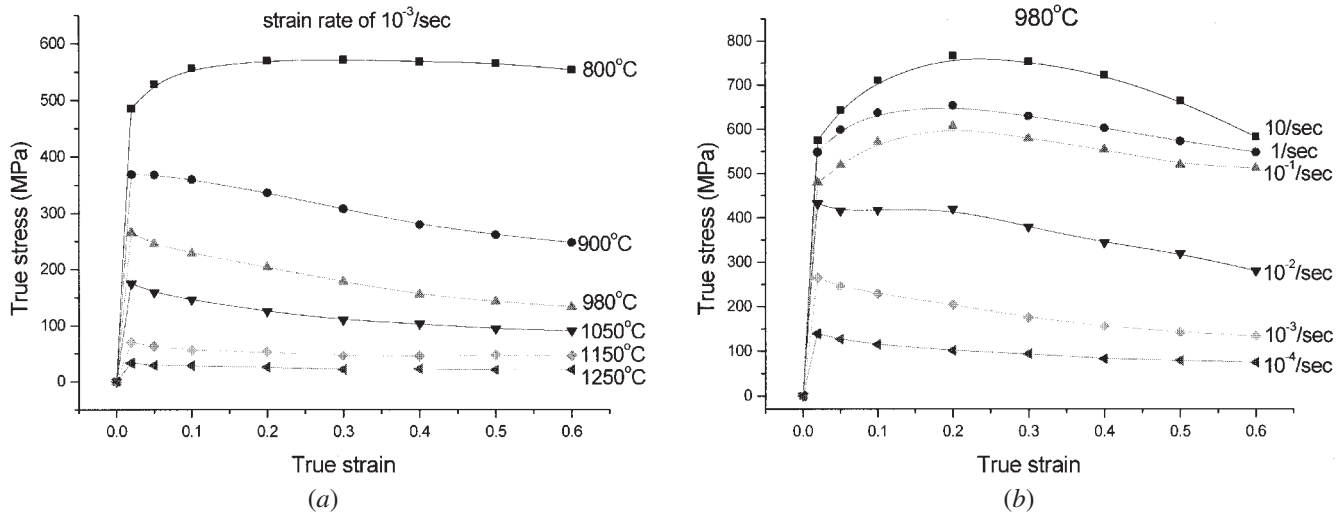

Fig. 5—True stress–true strain curves obtained from compression tests at (*a*) different temperatures (10^{-3}/s) and (*b*) different strain rates (980 °C).

C. *Processing Maps*

Processing maps are interpreted on the basis of the principles of the DMM,[11] which considers the workpiece deformed at high temperatures as a dissipater of power. The constitutive equation describes the manner in which the power is converted at any instant into two forms (thermal and microstructural forms), which are not recoverable by the system. The instantaneous power dissipated consists of two complementary parts: the *G* content, representing the temperature rise, and the *J* co-content, indicating the dissipation through metallurgical processes. The factor that partitions the power between *G*and *J* is the strain-rate sensitivity (m) of the flow stress (σ), and the *J* co-content is given by

$$J = \sigma\dot{\varepsilon}m/(m + 1) \qquad [9]$$

where $\dot{\varepsilon}$ is the strain rate. For an ideal linear dissipater, $m = 1$ and $J = J_{max} = \sigma\dot{\varepsilon}/2$. The efficiency of power dissipation of a nonlinear dissipater can be expressed as a dimensionless parameter,

$$\eta = J/J_{max} = 2m/(m + 1) \qquad [10]$$

This parameter is plotted as a function of temperature and strain rate to obtain the power-dissipation map. The efficiency represents the relative rate of internal entropy production during hot deformation and characterizes the dissipative microstructure under different temperature and strain-rate conditions. The DMM processing map is usually constructed using the flow curves obtained from the compression tests, not from the tensile tests. The data of tensile tests cannot be used since the flow behavior of materials would be largely affected by cavity formation, and flow stresses at a large amount of strain cannot be obtained in the tensile tests. Processing maps can also be generated using data from hot torsion tests. In this case, the safe domains are found to be unaffected. It is also well known that flow localization becomes more intense under shear-stress conditions.[36] A more-detailed description of developing the map was given in other articles on the basis of the DMM.[11,36]

In this study, power-dissipation maps were constructed using the aforementioned method, in the temperature range from 800 °C to 1250 °C and strain-rate range between 10/s and 10^{-4}/s. Figures 6(a) through (c) show the power-dissipation maps obtained at strains of 0.05, 0.2, and 0.6, respectively. It is noticed that the features of the map changed considerably with the strain. At relatively low temperatures (below 980 °C) and in the high-strain-rate regime (above 10^{-1}/s), the dissipation efficiency was very low in all cases.

Also, the distribution of the efficiency did not change significantly as the strain increased. On the contrary, at high temperatures (above 1050 °C) and in the low-strain-rate regime (below 10^{-2}/s), the dissipation efficiency was relatively high and the shape of the map was substantially changed. In the map of a strain of 0.05 (Figure 6(a)), there was only one domain showing a peak efficiency of 57 pct. When the strain increased to the levels of 0.2 and 0.6, the peak efficiency increased to 61 and 64 pct, respectively. However, it was also noted that another domain started to initiate at a region of 1000 °C and 10^{-3}/s (Figures 6(b) and (c)). At the strain of 0.6, a new domain represented a peak efficiency of 48 pct. This feature strongly suggests that microstructural changes occur during the deformation.

D. *Instability Map*

Ziegler[21] has shown that the condition for the plastic flow to become unstable is as follows:

$$\frac{dD}{d\dot{\varepsilon}} < \frac{D}{\dot{\varepsilon}}$$

where *D* is a dissipative function that is characteristic of the constitutive behavior of the material and is given by the dissipated power. If the power is separated into two parts, *G* and *J*, *D* may be replaced by the *J* co-content ($J = \sigma\dot{\varepsilon}m/(m + 1)$),

Table II. Flow Stress Values in MPa (Corrected for Adiabatic Temperature Rise) for Titanium Aluminide Alloy at Different Temperatures, Strain Rates, and Strains

Strain	Strain Rate (s)	Temperature (°C) 800	900	980	1050	1150	1250
0.05	10	672.1	663.3	643.7	619.3	510.3	319.0
	1	651.8	612.2	599.1	545.6	405.9	179.6
	10^{-1}	632.1	580.9	519.5	438.6	228.9	98.7
	10^{-2}	616.3	512.9	415.4	299.0	146.4	66.9
	10^{-3}	529.2	368.2	245.6	159.3	63.0	28.9
	10^{-4}	454.9	234.6	127.0	80.1	32.6	11.3
0.1	10	788.1	747.0	710.7	664.9	505.2	307.2
	1	743.5	689.1	637.5	545.7	377.3	164.2
	10^{-1}	738.7	660.3	571.8	476.4	245.5	102.6
	10^{-2}	706.0	547.9	417.6	278.4	131.8	59.6
	10^{-3}	557.3	359.9	229.1	146.0	55.9	28.5
	10^{-4}	455.5	223.4	114.9	74.3	31.1	10.9
0.2	10	936.3	840.9	766.9	667.3	443.9	264.6
	1	885.5	777.4	653.9	516.8	346.3	150.7
	10^{-1}	850.4	748.1	607.2	430.7	250.4	113.1
	10^{-2}	784.7	549.2	420.0	237.4	118.9	56.2
	10^{-3}	570.7	336.6	204.3	125.8	52.8	25.6
	10^{-4}	436.0	201.8	101.5	65.8	27.8	9.9
0.3	10	973.3	853.6	753.6	616.8	367.9	212.5
	1	920.2	810.9	629.7	475.1	317.1	140.3
	10^{-1}	880.2	768.7	579.4	360.2	232.8	110.3
	10^{-2}	819.5	518.6	379.5	200.3	108.4	53.3
	10^{-3}	572.1	308.1	178.5	110.5	46.1	21.7
	10^{-4}	420.6	176.0	94.1	58.4	26.0	9.3
0.4	10	900.0	822.2	722.7	569.8	342.8	159.8
	1	898.4	794.6	603.2	437.5	294.8	133.8
	10^{-1}	897.5	782.3	554.3	310.0	202.5	100.7
	10^{-2}	872.1	515.9	344.0	188.2	88.9	52.4
	10^{-3}	568.8	280.0	155.7	103.5	46.1	22.8
	10^{-4}	391.2	149.8	83.2	55.3	24.8	8.5
0.5	10	860.2	752.9	664.4	524.3	320.6	160.4
	1	851.8	760.3	573.4	406.5	282.0	130.0
	10^{-1}	845.5	771.4	520.3	276.7	175.9	94.7
	10^{-2}	838.1	498.1	319.5	150.2	82.6	48.6
	10^{-3}	566.2	261.7	143.2	94.7	47.4	20.9
	10^{-4}	357.9	134.3	79.3	54.3	25.8	8.1
0.6	10	806.5	630.5	582.9	461.9	283.6	159.8
	1	791.2	626.3	548.3	390.0	273.9	128.0
	10^{-1}	777.1	725.9	512.3	268.8	154.8	89.3
	10^{-2}	756.6	479.7	280.5	176.5	81.7	49.3
	10^{-3}	554.1	247.9	133.9	91.1	46.6	21.2
	10^{-4}	341.2	137.9	75.2	52.1	27.9	7.2

which represents the power dissipation occurring through the microstructural changes. Hence, Eq. [11] becomes

$$\frac{\partial \ln\left(\frac{m}{m+1}\right)}{\partial \ln \dot{\varepsilon}} + m < 0 \qquad [12]$$

The left-hand side of Eq. [12] is denoted by $\xi(\dot{\varepsilon})$, which, when negative, indicates microstructural instability in the material.

The $\xi(\dot{\varepsilon})$ variation as a function of strain rate and temperature is evaluated and represented in Figure 7 as an instability map at a strain of 0.6. The criterion predicts a regime of flow instability at strain rates higher than 1/s over the entire test-temperature range. Here, the flow instability includes all kinds of nonuniform metal flow on a macro or micro scale. These predictions have been validated with microstructural observations. The notation "C" means surface cracking, and the notation "U" represents unsound deformation such as shear localization, a grain-boundary cavity, or intergranular cracking.

V. DISCUSSION

A. *Processing map at a strain of 0.6*

The map (Figure 6(c)) exhibits two clear domains where the efficiency of power dissipation has reached the local maximum in a significant way, and they are at (1) 980 °C and 5×10^{-3}/s with a peak efficiency of about 48 pct and (2) 1250 °C and

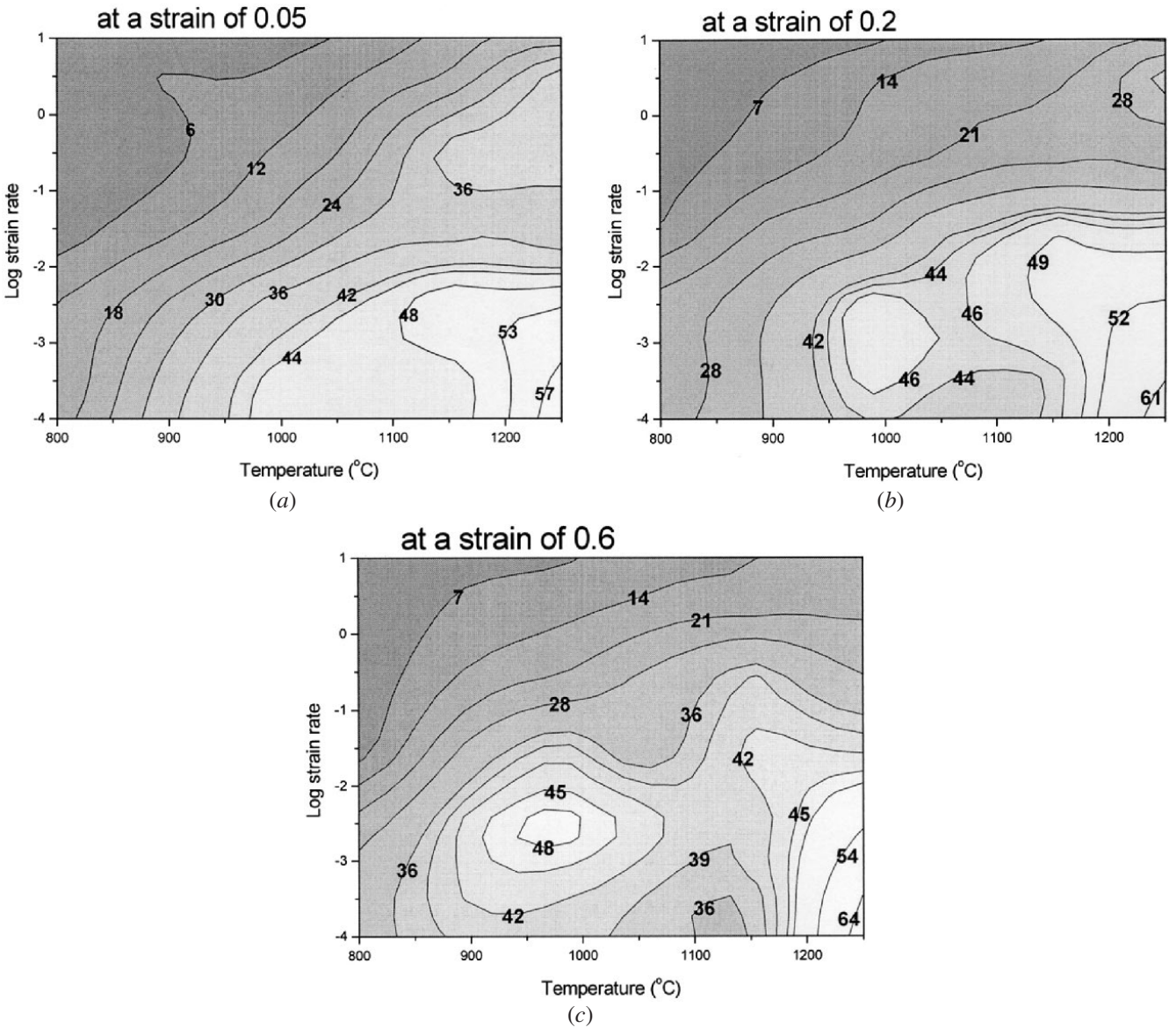

Fig. 6—Power dissipation efficiency maps obtained for TiAl alloy at strains of (*a*) 0.05, (*b*) 0.2, and (*c*) 0.6. Contour numbers represent percent efficiency of power dissipation.

10^{-4}/s with a peak efficiency of about 64 pct. These are identified as domains of DRx and superplasti-city, respectively.

1. *Domain at 980 °C and 5 × 10^{-3}/s*

This domain occurs in the homologous temperature range around 0.7 T_m, and the widely spaced contours indicate a less-steep hill. These are typical features of DRx.[36] Figure 8 shows microstructures of specimens deformed at 980 °C up to a strain of 0.6, using different strain rates. With a strain rate of 10^{-1}/s (Figure 8(a)), the microstructure showed elongated grains, indicating that the dislocation-glide process took place as predicted in the load-relaxation results. It can be clearly seen that grain refinement took place during deformation at the high-temperature and low-strain-rate regime (980 °C and 10^{-3}/s, 980 °C and 10^{-4}/s, and 1050 °C and 10^{-3}/s) due to the occurrence of DRx, as shown in Figures 8(b) through (d). The extent of grain refinement is highest at 980 °C and 10^{-3}/s; this microstructural observation clearly indicates that the domain at 980 °C and 5 × 10^{-3}/s arises from the DRx process. This domain is recommended for optimum hot-working conditions, because DRx not only gives good intrinsic workability by simultaneous softening, but also converts the microstructure.[36]

Previous investigations have reported that the deformation efficiency for DRx is closely related to the stacking-fault energy of an alloy, as well as its composition and crystal structure. For low-stacking-fault-energy materials such as Cu and Ni,[22,23] the DRx domain is found at high homologeous temperatures (0.7 to 0.8T_m) and intermediate strain rates (1 to 10^{-1}/s) with a maximum dissipation efficiency of 30 to 40 pct. On the other hand, the DRx domain of high-stacking-fault-energy materials such as Al and Cd[11,27] appears in the region of low strain rates (10^{-2} to 10^{-3}/s) with a maximum dissipation efficiency of 50 to 55 pct. The relations between the strain-rate-induced DRx process and the stacking-fault energy of several materials are represented in Figure 9.[11,22–27] Single-phase γ-TiAl is considered a

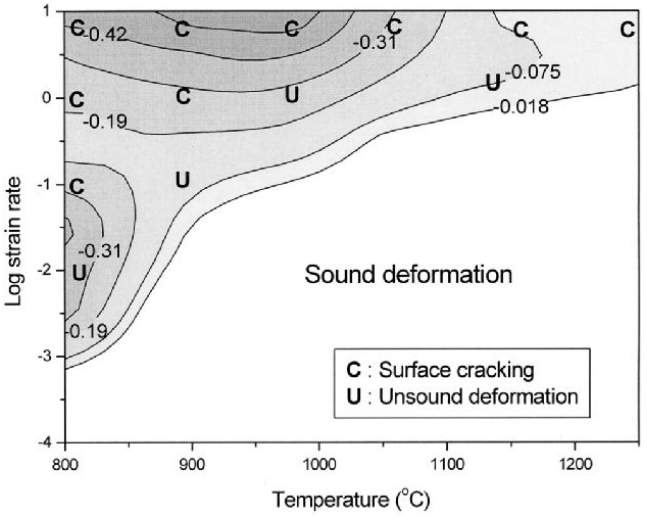

Fig. 7—Instability map of TiAl alloy obtained at a strain of 0.6. Contour numbers represent the value of instability parameter given by Eq. [10].

low-stacking-fault-energy material (60 to 90 mJ/ m^2).[28,29,30] As such, it is expected that the strain rate for DRx would be high. According to earlier work on a near-gamma TiAl alloy,[20] the volume fraction of recrystallized grains increased with strain rate from about 45 pct for $\dot{\varepsilon} = 10^{-3}$/s to 75 pct for $\dot{\varepsilon} = 10^{1}$/s at 1000 °C after deformation to $\varepsilon \cong 0.7$. At the same time, the mean grain size also decreased as the strain rate increased to 10^{1}/s. Sabinash *et al.*[32] have also reported similar results on single-phase material. These results for single γ-phase material fit the trend shown in Figure 9.

The material used in this study had a large volume fraction of γ phase, which was about 90 pct. It was, therefore, expected that grain refinement would be significant at relatively high strain rates. However, our results showed the opposite trend, resulting in a high peak-efficiency value (48 pct at a strain of 0.6) at relatively low stain rates. This feature suggests that duplex TiAl behaves like a high-stacking-fault-energy material, which is primarily due to the presence of α_2 and β phases. The exact value of the stacking-fault energy of α_2 phase in TiAl is still not available, but is considered high on the basis of its similarity to

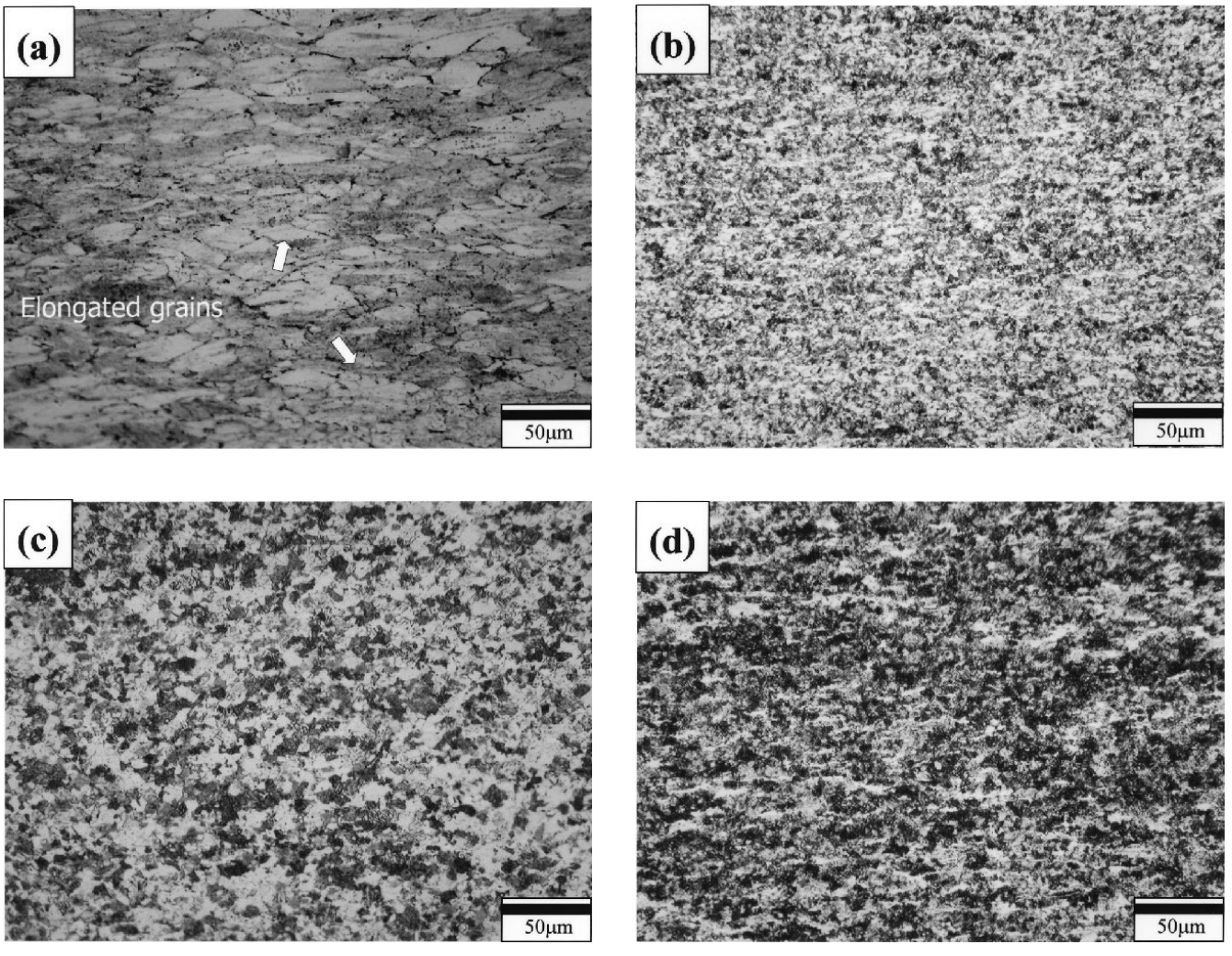

Fig. 8—Microstructures of TiAl specimen deformed up to a strain of 0.6 at 980 °C: (*a*) 10^{-1}/s, (*b*) 10^{-3}/s, (*c*) 10^{-4}/s, and (*d*) 1050 °C, 10^{-3}/s. The compression axis is vertical.

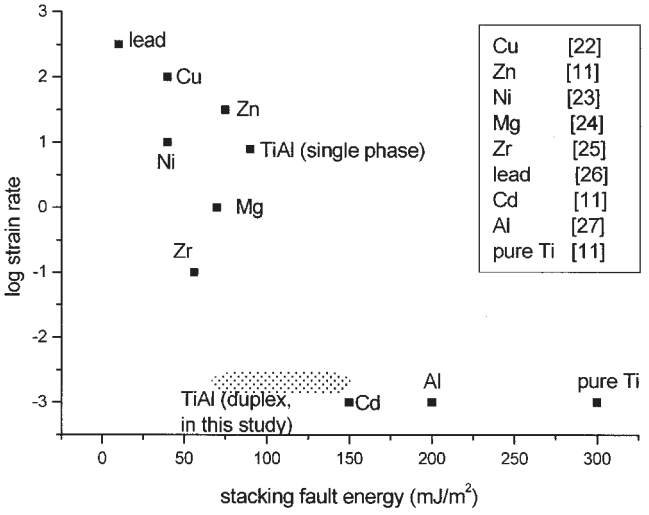

Fig. 9—Relationship between strain rate for dynamic recrystallization and stacking fault energy of various materials.

the Ti_3Al alloy. Other work has reported that the DRx domain of the α_2 phase in Ti_3Al (Ti-25Al-15Nb) is located in the region of 10^{-3}/s,[31] which is sufficiently low for it to be thought of as a high-stacking-fault-energy material. Figure 10(a) shows an optical micrograph of a specimen deformed at 980 °C and 10^{-2}/s. It appears that both the α_2 and γ grains were considerably recrystallized. It was thought that the moving boundaries during the DRx were within each phase (γ, α_2, and β phase). However, α_2 grains were not fully recrystallized and nonuniformly distributed, because the strain rate of this experiment was so high that the α_2 phase could not be fully recrystallized. Figure 10(b) shows a BSE micrograph of a specimen deformed using the same conditions. It also shows that the α_2 (gray) and β (white) grains were elongated along the direction perpendicular to the compression axis and not uniformly distributed.

In spite of the small volume fraction of α_2 and β phases, they seem to have a significant influence on the DRx behavior of the duplex TiAl alloy, because they were finely dispersed as particles or films between γ grain boundaries (Figure 2(b)). Thus, nucleation of new grains at γ grain boundaries can be effectively suppressed at high strain rates. Thus, it is expected that the hot-workability limit of two-phase alloys (which contain α_2 phase) is less than that of the single γ-phase alloys; this expectation has been confirmed by Nobuyuki[9] and Fujitsuna *et al.*[33] However, the workability of single-phase γ-alloys may not be always better than that of two-phase alloys, because two-phase alloys have a higher efficiency of dissipation at the DRx regime and are better inhibitors of grain growth during hot working. Thus, the α_2-phase volume fraction should be controlled carefully, considering such a problem.

2. *Domain at 1250 °C and 10^{-4}/s*

This domain typically shows a region of superplasticity or wedge cracking,[36] which can occur at temperatures of 0.7 to $0.8T_m$ and strain rates lower than 10^{-3}/s. Both processes are characterized by a high efficiency of power dissipation (above 60 pct) and a steep rise of efficiency

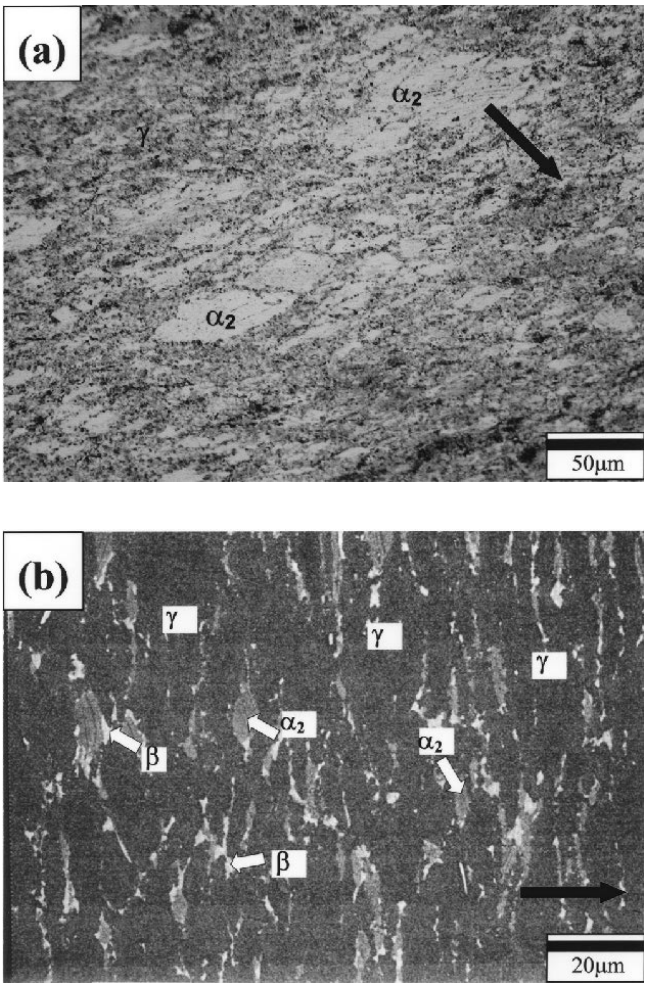

Fig. 10—Micrographs of specimen deformed up to a strain of 0.6 at 980 °C, 10^{-2}/s: (*a*) optical image and (*b*) backscattered electron image. The dark arrow indicates the compression axis.

with decrease of strain rate. Figure 11 shows the microstructure of a specimen deformed (up to a strain of 0.6) at 1250 °C and 10^{-4}/s, in which wedge cracking was not observed. The value of strain-rate sensitivity at this test condition is about 0.5, which is characteristic of superplastic materials. Mukherjee *et al.* have reported a large elongation of 330 pct at 1250 °C and 8×10^{-5}/s, which are very similar conditions to those where the domain was observed.[35] Also, the grains in Figure 11 show distinct boundaries, which would promote the operation of GBS. Thus, it is considered that the domain relates to a superplastic deformation region.

Figure 11 shows some twinning structures in the γ phase. Deformation twinning is generally believed to occur at low temperatures below 750 °C and at stresses over 200 MPa in the lamellar structure,[34] which is far away from this test condition. From the shape of the twins, they are considered to be annealing twins. It is not clear whether they are from the initial microstructures (Figure 2) or if they are new ones formed during deformation. It is interesting to notice that the deformed microstructure shown in Figure 11 is similar to the initial microstructure shown in Figure 2, revealing no change of grain size and shape, which is one of the typical

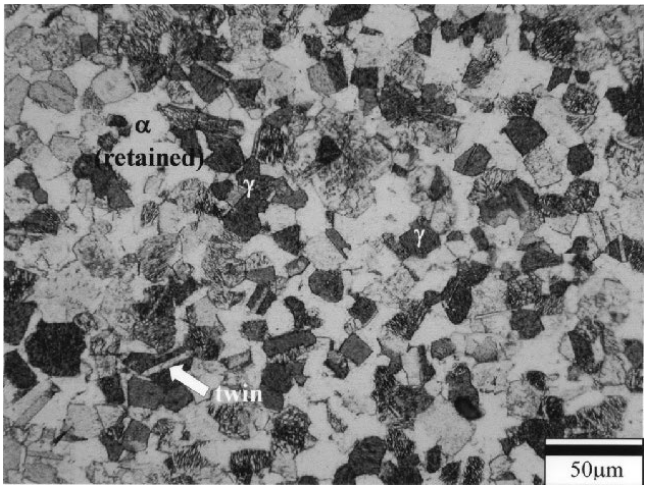

Fig. 11—Microstructures of TiAl specimen deformed up to a strain of 0.6 at 1250 °C and 10^{-4}/s. The compression axis is vertical.

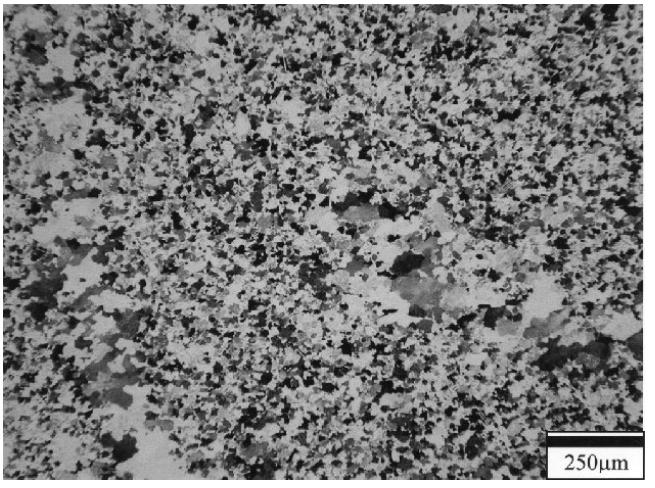

Fig. 12—Microstructures of TiAl specimen deformed up to a strain of 0.6 at 1150 °C and 10^{-4}/s. The compression axis is vertical.

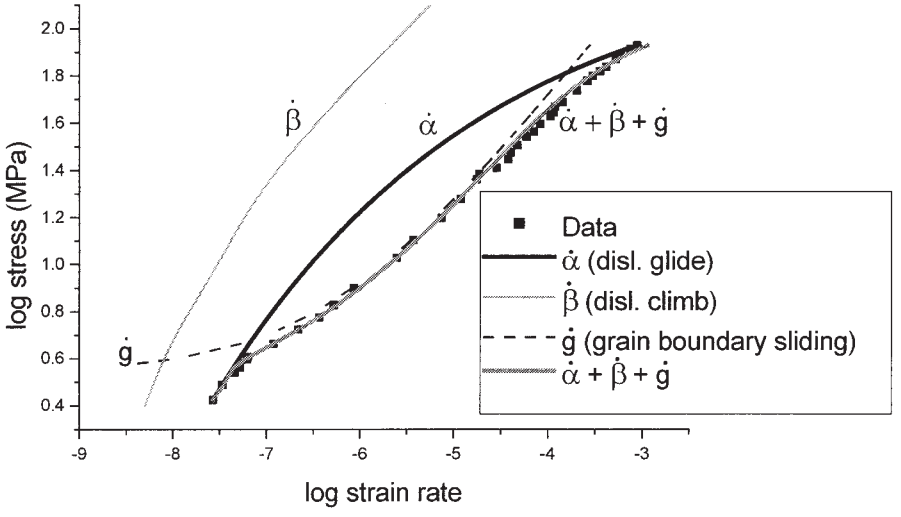

Fig. 13—The flow curves of prestrained ($\varepsilon \cong 0.8$) specimen at 980 °C. The notations of $\dot{\alpha}$, $\dot{\beta}$, and $\dot{g}$ denote the strain rates of dislocation glide, dislocation climb, and grain boundary sliding, respectively.

characteristics of superplastic deformation. If superplastic deformation prevails in this region, twins from the initial microstructures can still remain, because there would be no significant GMD.

Figure 6(c) shows that the efficiency of dissipation at low strain rates increases steeply as the temperature increases from 1150 °C to 1250 °C. This steep increase of the efficiency is attributed to (1) phase transformation ($\alpha_2 + \gamma \rightarrow \alpha$) occurring at about 1150 °C and (2) the increase of α phase. The α phase is thought to accommodate the applied strains at triple junctions by slip deformation and to inhibit grain growth by enveloping the γ grains.[35] Thus, it is proposed that the relatively high efficiency arises from GBS promoted by the increase of α phase.

On the other hand, the efficiency of dissipation at 10^{-4} and 1150 °C is relatively low and decreases as the strain increases. This temperature is supposed to be near the phase-transformation temperature, where the α-phase volume fraction is not enough to prevent grain growth of γ phase. Figure 12 shows the microstructure of a specimen deformed up to a strain of 0.6 under these conditions. Abnormal grain growth of the γ phase is observed, with a coarse grain size of about 100 μm. From this observation, it is concluded that the decrease in efficiency of power dissipation at this region is caused by significant abnormal grain growth of the γ phase, which is due to long-time exposure at high temperatures and a lack of α phase.

B. *Deformation Mechanisms*

From the load-relaxation tests and the analyses using the internal-variable theory, the high-temperature deformation mechanisms of a fine-grained duplex TiAl alloy at an infinitesimal strain level have been found to be GMD due to dislocation glide and dislocation climb. It should be noted that the GMD due to dislocation climb is expected only in the very low-strain-rate region and at high temperatures above 980 °C. As shown in the processing maps of Figure 6, on the other hand, additional deformation mechanisms such as DRx and superplasticity appeared to operate at the finite-strain level.

Interestingly, superplasticity was observed to occur at 1250 °C and 10^{-4}/s. Although load-relaxation tests at this temperature could not be performed from the experimental constraints, typical microstructural features, *i.e.*, unchanged grain size and deformation-free grain matrices due to GBS, were observed. It is well known that refinement of the grain size reduces the temperature and, simultaneously, increases the strain rate for superplastic deformation. From the processing map, DRx was expected to occur at the strain rate of 10^{-3}/s and the temperature of 980 °C, which was also confirmed by the microstructural observation of a deformed specimen. For the specimen predeformed under these conditions ($\varepsilon \cong 0.8$), additional load-relaxation tests were conducted at 980 °C, and the results are given in Figure 13. An entirely different shape of the log stress-*vs*-log strain-rate curve, with a broad concave region at the intermediate-strain-rate region, is obtained. The manifestation of the concave portion in the flow curve means that the material is superplastic, according to the internal-variable theory. It is, therefore, concluded that the grain refinement through DRx definitely enhanced the superplasticity of the TiAl alloy.

C. *Flow Instabilities*

Metallurgical instabilities, as predicted by the instability map presented in Figure 7, were investigated using optical macro/microscopy. Figure 14 shows the appearance of the compression-test specimens deformed under different conditions. Surface cracking appeared in the specimen deformed at 980 °C and 10/s because of the severe deformation condition, and this cracking results in power dissipation, which corresponds to a rapid decrease of the flow stress under this test condition, as shown in Figure 5(b). In contrast, the specimen tested at 1250 °C and 10^{-3}/s was soundly deformed.

Figure 15(a) shows that intergranular cracking occurred at 800 °C and 10^{-2}/s, where the value of the instability parameter is as low as -0.31. Although there is no surface cracking, this phenomenon is very harmful to the mechanical properties of the material. Thus, this region should be avoided during the hot-working process. In Figure 15(b), the microstructure of the specimen deformed at 900 °C and 10^{-1}/s exhibited flow localization (dark bands in the micrograph), which is not recommended either. The aforementioned macro/micro structural observations show very good agreement with the instability criterion of a TiAl alloy.

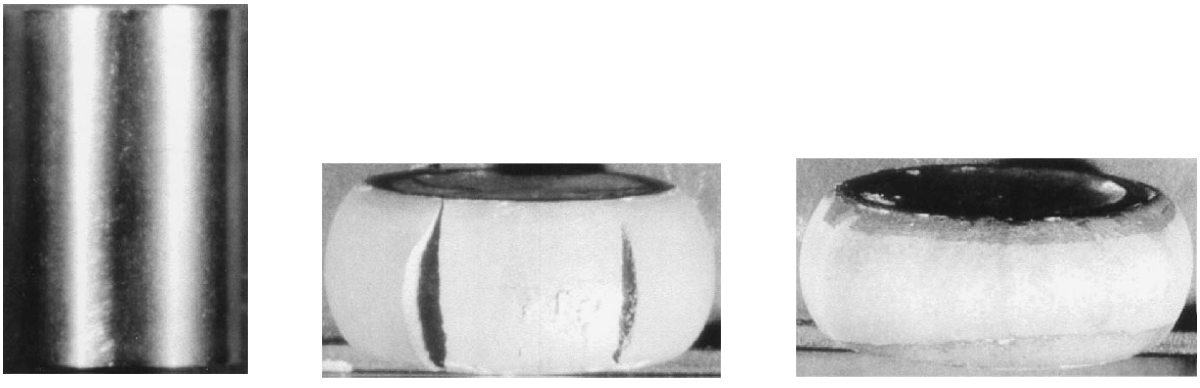

(*a*) (*b*) (*c*)

Fig. 14—Appearance of the compression testing specimens: (*a*) undeformed specimen, (*b*) surface cracked specimen deformed at 980 °C and 10/s, and (*c*) soundly deformed specimen at 1250 °C and a strain rate of 10^{-3}/s.

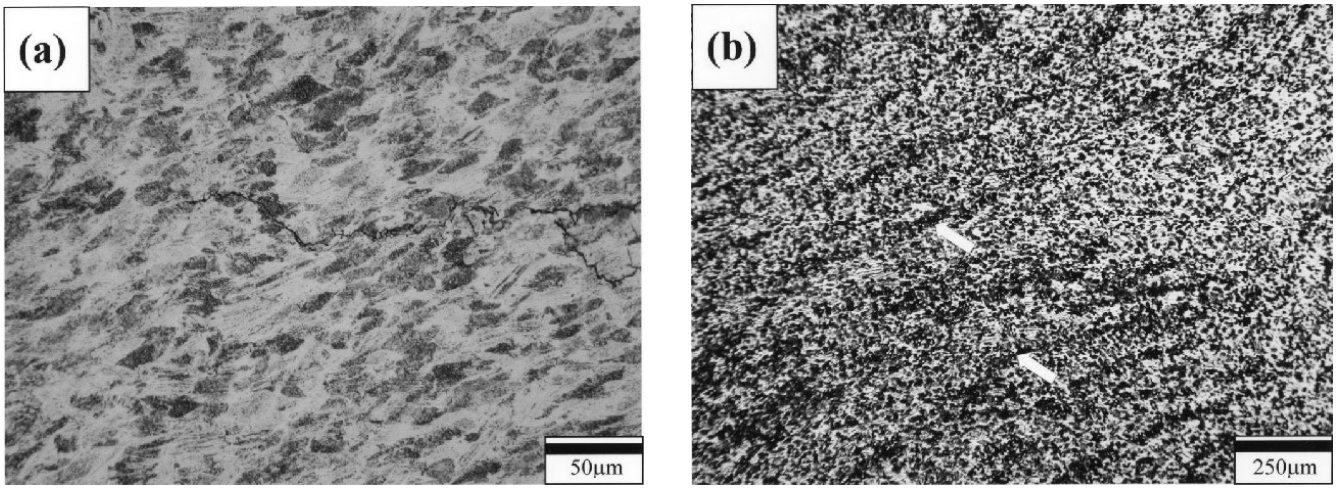

Fig. 15—Microstructure of TiAl alloy specimen deformed at (*a*) 800 °C and 10^{-2}/s and (*b*) 900 °C and 10^{-1}/s, exhibiting intergranular cracking and flow localization, respectively. The compression axis is vertical.

VI. CONCLUSIONS

Load-relaxation tests and hot-compression tests for a duplex TiAl alloy were conducted under various test conditions, and the results were analyzed using the internal-variable theory of inelastic deformation and the DMM. The following conclusions were drawn from this investigation.

1. When a small amount of strain ($\varepsilon \cong 0.05$) was imposed, as in the load-relaxation test, the constitutive behavior of the fine-grained TiAl alloy agreed well with the combined curves of dislocation glide and dislocation climb. With an increase of strain, DRx took place, resulting in grain refinement, which made GBS boundary sliding prevalent. In turn, the stress *vs* strain-rate response of heavily deformed material ($\varepsilon \cong 0.8$) was well matched with the combined curves of dislocation glide and GBS.
2. Processing maps at strain levels of 0.05, 0.2, and 0.6 were drawn for the duplex Ti-Al alloy. With an increase of strain, two domains became apparent, *i.e.*, DRx and superplasticity, which were identified through microstructural observation. The DRx occurred most extensively at 980 °C and 5×10^{-3}/s, with a peak efficiency of 48 pct, and superplastic deformation occurred most at 1250 °C and 10^{-4}/s, with a peak efficiency of 64 pct.
3. Instability conditions were predicted by constructing an instability map. Instability processes such as surface cracking, intergranular cracking, and flow localizations were observed, and took place under conditions in accordance with the instability map.

ACKNOWLEDGMENT

The authors are thankful to Dr. Y.-W. Kim (UES, Inc.) for providing the gamma-TiAl alloy used in this study.

REFERENCES

1. Y.-W. Kim: *J. Met*., 1995, vol. 47, pp. 39-41.
2. R.W. Hayes and B. London: *Acta Metall*., 1992, vol. 40, p. 2167.
3. P.L. Martin, M.G. Mendiratta, and H.A. Lipsitt: *Metall. Trans. A*, 1983, vol. 14A, p. 2170.
4. Y.-W. Kim and F.H. Froes: in *High Temperature Aluminides and Intermetallics*, S.H. Wang *et al*., eds., TMS, Warrendale, PA, 1990, pp. 465-92.
5. S.C. Huang and E.L. Hall: *Metall. Trans. A*, 1991, vol. 22A, p.427.
6. S.L. Semiatin, D.C. Vollmer, S. El-Soudani, and C. Su: *Scripta Metall. Mater*., 1991, vol. 25, p. 1409.
7. H.E. Deve, A.G. Evans, and D.S. Shih: *Acta Metall. Mater*., 1992, vol. 40, p. 1259.
8. T. Kawabata, T. Kanai, and O. Izumi: *Acta Metall. Mater*., 1985, vol. 33, pp. 1355-66.
9. M. Nobuki and T. Tsujimoto: *Iron Steel Inst. Jpn. Int*. 31 (1991), pp. 931-937.
10. T.K. Ha and Y.W. Chang: *Acta Mater*. 1998, vol. 46, p. 2741.
11. Y.V.R.K. Prasad and S. Sasidhara: *Hot Working Guide—A Compendium of Processing Maps*, ASM INTERNATIONAL, Materials Park, OH, 1997.
12. J.S. Kim, Y.W. Chang, and C.S. Lee: *Metall. Mater. Trans. A*, 1998, vol. 29A, p. 217.
13. J.S. Kim, W.J. Nam, and C.S. Lee: *Met. Mater*., 1998, vol. 4, p. 1041.
14. D. Lee and E.W. Hart: *Metall. Trans*., 1971, vol. 2, pp. 1245-48.
15. T.K. Ha, H.J. Sung, K.S. Kim, and Y.W. Chang: *Mater. Sci. Eng*. 1999, vol. 271, p. 166.
16. F. Appel, U. Lorenz, M. Oehring, U. Sparka, and R. Wagner: *Mater. Sci. Eng. A*, 1997, vol. 233 (1–2).
17. W.J. Zhang, Z.C.C. Liu, G.L. Chen, and Y.-W. Kim: *Mater. Sci. Eng*., 1999, vol. A271, pp. 416-23.
18. T.K. Ha and Y.W. Chang: *Scripta Mater*., 1996, vol. 35, p. 1317.
19. J.S. Kim, J.H. Kim, Y.T. Lee, C.G. Park, and C.S. Lee: *Mater. Sci. Eng. A*, 1999, vol. A263, pp. 272-80.
20. V. Seetharaman and C.M. Lombard: in *Microstructure/Property Relationships in Titanium Aluminides and Alloys*, Y.-W. Kim and R.R. Boyer, eds., TMS, (Warrendale, PA, 1991), pp. 237-51.
21. H. Ziegler: in *Progress in Solid Mechanics*, I.N. Sneddon and R. Hill, eds., Wiley, New York, NY, 1965, vol. 4, pp. 91-193.
22. N. Ravichandran and Y.V.R.K. Prasad: *Mater. Sci. Eng*., 1992, vol. A156, p. 195.
23. N. Srinivasan and Y.V.R.K. Prasad: *Mater. Sci. Technol*., 1992, vol. 9, p. 206.
24. O. Sivakesavam, I.S. Rao, and Y.V.R.K. Prasad: *Mater. Sci. Technol*., 1993, vol. 9, p. 805.
25. J.K. Chakravarty, Y.V.R.K. Prasad, and M.K. Asundi: *Metall. Trans. A*, 1991, vol. 22A, pp. 829-36.
26. J.A. Bailey and A.R.E. Singer: *J. Inst. Met*., 1963–64, vol. 92, p. 404.
27. N. Ravichandran and Y.V.R.K. Prasad: *Metall. Trans. A*, 1991, vol. 22A, pp. 2339-48.
28. G. Hug, A. Loiseau, and P. Veyssiere: *Phil. Mag*., 1988, vol. 57, p. 499.
29. J. Panova and D. Farkas: in *Gamma Titanium Aluminides*, Y.-W. Kim, R. Wagner, and M. Yamaguchi, eds., TMS, Warrendale, PA, 1995, pp. 331-38.
30. D.G. Morris, S. Gunter, and M. Leboeuf: *Phil. Mag. A*, 1994, vol. 69, p. 527.
31. P.K. Sagar and Y.V.R.K. Prasad: *Z. Metall*., 1998, vol. 89 (6), pp. 433-41.
32. C.M. Sabinash, S.M.L. Sastry, and K.L. Jerina: *Mater. Sci. Eng. A*, 1995, vols. A192–A193, pp. 837-47.
33. N. Fujitsuna, H. Ohyama, Y. Miyamoto, and Y. Ashida: *Iron Steel Inst. Jpn. Int*., 1991, vol. 31 (10), pp. 1147-53.
34. M.A. Morris and M. Leboeuf: *Intermetallics*, 1997, vol. 5, pp. 339-54.
35. W.B. Lee, H.S. Yang, Y.-W. Kim, and A.K. Mukherjee: *Scripta Metall*., 1993, vol. 29, pp. 1403-08.
36. Y.V.R.K. Prasad and T. Seshacharyulu: *Int. Mater. Rev*., 1988, vol. 43 (6), pp. 244-58.